A Depolarization Ratio Anomaly Detector to identify icebergs in sea ice using dual-polarization SAR images

Armando Marino, *Member, IEEE*, Wolfgang Dierking, Christine Wesche.

ABSTRACT

Icebergs represent hazards to maritime traffic and offshore operations. Satellite Synthetic Aperture Radar (SAR) is very valuable for the observation of polar regions and extensive work was already carried out on detection and tracking of large icebergs. However, the identification of small icebergs is still challenging especially when these are embedded in sea ice. In this work, a new detector is proposed based on incoherent dual-polarization SAR images. The algorithm considers the limited extension of small icebergs, which are supposed to have a stronger cross polarization and higher cross- over co-polarization ratio compared to the surrounding sea or sea ice background.

The new detector is tested with two satellite systems. Firstly, RADARSAT-2 quad-polarimetric images are analyzed to evaluate the effects of high resolution data. Subsequently a more exhaustive analysis is carried out using dual-polarization ground detected Sentinel-1a Extra

Armando Marino is with the Open University, Engineering and Innovation, Milton Keynes, United Kingdom (e-mail: armando.marino@open.ac.uk). Wolfgang Dierking and Christine Wesche are with the Alfred-Wegener-Institut fuer Polar- und Meeresforschung, Am Handelshafen 12, 27570 Bremerhaven, Germany. Wolfgang Dierking is also with the Arctic University of Norway, Hansine Hansens veg 18, 9019 Tromsø

Wide swath images acquired over the time span of two months. The test areas are on the East Coast of Greenland, where several icebergs have been observed.

A quantitative analysis and a comparison with a detector using only the cross polarization channel is carried out exploiting grounded icebergs as test targets. The proposed methodology improves the contrast between icebergs and sea ice clutter by up to 75 times. This returns an improved probability of detection.

I. Introduction

Synthetic Aperture Radar (SAR) provides images of the microwave reflectivity of the Earth's surface. SAR instruments are highly valuable for monitoring polar regions since they do not rely on solar illumination and can operate almost independently of cloudiness [1]. Hence, they are optimal for iceberg monitoring from space. In this paper, we discuss a new method to detect icebergs by combining SAR images acquired in co-polarization (HH) and cross-polarization (HV), hence considering that the radar signal obtained from icebergs is in most cases dominated by volume scattering and/or multiple reflections, whereas signal characteristics from open water and saline sea ice are mainly determined by surface scattering [2], [3], [4].

The Greenland ice sheet loses mass due to melting and to accelerated ice flow. This dynamic thinning has been monitored over the entire ice sheet using repeated data acquisitions from satellite altimetry [5]. The thinning is higher at the margins of the marine-terminating glaciers, the birthplaces of icebergs [6].

One of the largest tidewater glaciers in Greenland is the Helheim Glacier in southeastern Greenland. Calving occurs year-round at the 6 km wide calving front into Helheim Fjord, which is a lateral branch of Sermilik Fjord. Due to the highly crevassed front of the Helheim

glacier, only a few tabular icebergs were observed to calve. Most calving events create smaller icebergs that topple in- or outward [6]. For the study presented in this paper, we selected Helheim Glacier as one of our test sites.

In SAR images, icebergs are often (but not always) visible as bright targets. Under freezing conditions in calm open water or young undeformed sea ice, the radar signature contrast between icebergs and the background clutter (i. e. the radar reflectivity of open water or smooth sea ice) is high enough for an automated detection using single-polarization SAR imagery [7], [8], [9]. Since smaller icebergs that calve from Helheim Glacier or any other marine-terminating glacier in Greenland or Antarctica tend to topple in open water, their backscattering characteristics change because the ice surface is wet or covered by frozen sea water. If the iceberg capsizes, the surface may consist of a layer of marine ice that formed the bottom layer before the berg calved. In this case, the contrast between iceberg and clutter is very small, so that an automated detection of icebergs using single-pol imagery is nearly impossible [7]. The success of detection depends also on the spatial resolution of the SAR image and the areal extension of the iceberg. Icebergs are more difficult to identify if they cover only a few image pixels, and cannot reliably be detected if their size is close to or even smaller than the image resolution.

A hemispheric wide systematic iceberg detection is not existent, but studies focusing on different regions were published. E.g., Abramov [10] reports on iceberg observations in the Barents Sea carried out from ships and during reconnaissance flights that were conducted by the Russian Arctic and Antarctic Research Institute (AARI) between 1933 and 1990. The Danish Meteorological Institute (DMI) investigated the iceberg frequencies in open waters in the Disco Bay (West Greenland) and Scoresbysund (East Greenland) using more than 8000 SAR scenes (most of them acquired after 2009). For the automated detection, they applied

a constant false alarm rate technique [11]. A maritime monitoring service for the Canadian Arctic is offered by C-CORE, a Canadian research and development cooperation. They have been developing software for iceberg detection and classification in SAR images taking advantage of the dual- and quad-polarization capabilities of modern SAR systems. However, details about their method are not provided [12]. Andres et al. [13] present a different approach of detecting icebergs. Here, inverted echo sounders equipped with pressure sensors were installed in Sermilik Fjord between August 2011 and September 2012. These sounders are able to distinguish iceberg and sea ice by their draft [13]. Although this method is spatially limited to the locations where the instruments were deployed, and does not detect bergs passing through the spatial gaps between the sounders, it is useful to identify icebergs for validating the detection algorithms developed for SAR images.

The paper is organized as follows. Section I provides a brief introduction on iceberg detection and polarimetric radar. Section II introduces the new detector that is tested with RADARSAT-2 and Sentinel-1 data in Section III and IV respectively.

A. Iceberg Detection

An ordinary approach to iceberg detection considers the exploitation of algorithms previously developed for ship detection. More specifically, several of these methodologies aim at discriminating between targets and background clutter performing a statistical test on the image brightness. The problem of selecting the threshold can be solved using the Neyman-Pearson lemma on the probability of detection (P_d) or false alarms (P_f) [14]. The most common methodology is called constant false alarm rate (CFAR) and set a threshold that is supposed to keep P_f constant [15], [16], [17], [18], [19], [20], [21], [22], [23]. CFAR algorithms are generally (but not necessarily) applied to single intensity images. When only a

single image is available, one important advantage of using a CFAR methodology, compared to setting a global threshold, is that the detection task becomes more automatic. The CFAR is capable of setting the threshold locally by extracting the clutter statistics. However, it is important to keep in mind that the performance of a CFAR is dependent on the suitability of the statistics employed to fit the clutter. A disadvantage of CFAR on single intensity image is that they do not perform any image enhancement based on some physical rational. To compensate for this the CFAR algorithms can be applied on one image that has been previously enhanced using different polarimetric channels (as in this work).

The proposed detector makes use of two differently polarized channels. The use of different polarizations is expected to add information because different targets are supposed to exhibit different polarimetric behaviors [24]. Therefore, the differences between clutter and targets can be magnified based on the responses at different polarizations, which helps detection or classification [25], [26], [27], [28], [29], [30], [31].

In this work, we focus on the particularly challenging condition of medium and small icebergs embedded in sea ice. Although the detection of icebergs of several kilometers size is routinely done, there are still issues in identifying icebergs smaller than a few hundred meters, especially when embedded in sea ice [4], [32], [3], [2]. To be in accordance with the detection jargon, in the following the sea ice background will be referred as clutter. Sea ice is expected to exhibit a high level of clutter (i.e. bright background) in several cases. This has two main drawbacks for single polarization detectors:

(1) If the algorithm sets the threshold globally, a very bright clutter can trigger detections. This introduces false alarms.

(2) If the algorithm sets the threshold locally (based on the background level) the high clutter brightness returns very high thresholds that may miss icebergs. This introduces missing

detections.

By using different polarizations, we want to add more physical information that can increase the contrast between targets and clutter.

B. Polarimetric Radar

In the following, a very brief introduction to polarimetry is presented, with the mere purpose of introducing the symbolism used in the following. A single target has a fixed polarization in time/space and we can characterize it using the scattering (Sinclair) matrix or equivalently a scattering vector $\underline{k}$ [24]. This is normally represented as

$$[S] = \begin{bmatrix} HH & HV \\ VH & VV \end{bmatrix}, \tag{1}$$

where *H* stands for linear horizontal and *V* for linear vertical (therefore the *HV* image is obtained transmitting a linear vertical polarization and receiving the linear horizontal one). The diagonal elements are often referred to as co-polarization channels and the off-diagonal are the cross-polarization channels. The full scattering matrix can be acquired only with quad-polarimetric data. When only two polarization channels are available, the mode is referred to as dual-polarimetric if the channels are coherent (i. e. their complex correlation coefficient can be determined) or dual-polarization if data acquisition is incoherent. The targets observed by a SAR system are often distributed and composed of different objects. For this reason, each pixel of such distributed targets may have a specific polarimetric behavior. In order to extract meaningful information regarding the polarimetric behavior averaging (or filtering) is required [24]. This is also valid if only the intensity of the polarimetric channel is available.

Unfortunately, currently radar satellites (including RADARSAT-2, ALOS-2, TanDEM-X

and Sentinel-1) can only provide very large swaths with dual-polarization data [33]. This is a limitation for applications as iceberg detection, since the use of large swaths is fundamental. For this reason, we propose a detector combining the HH- and HV-polarized intensity data. On the other hand, it is expected that the use of quad-polarimetric data can improve the detection performance. In the future, the availability of polarimetric images with large swaths may provide significant improvements in iceberg detection for operational purposes.

II. Dual-Pol Ratio Anomaly Detector (DPolRAD)

A. Dimensionless detector

In this section, a new algorithm is proposed for the detection of small icebergs embedded in sea ice. The design is based on the idea of producing a methodology that could be eventually used operationally. At the moment, there are two clear constraints for operational algorithms:

(1) Data availability: we need to exploit acquisition modes able to cover large areas (e.g. Sentinel-1 Extra Wide). Therefore, only dual-polarization incoherent HH/HV or VV/VH images can be used.

(2) Processing burden: an operational detector should be fast and not excessively reliant on high processing burden. For this reason, we tried to develop an algorithm that is efficient and fast.

The algorithm is based on the observation that icebergs or thick/deformed sea ice exhibit a different polarimetric behavior compared to thinner sea ice. Specifically, the cross polarization channel and the ratio between cross- and co-polarizations (here referred as depolarization ratio) increase. There are several physical explanations for such observations [4]. Icebergs are made of fresh water ice that in dry conditions has a much lower dielectric

loss compared to sea ice. This allows for a much larger penetration of electromagnetic waves in the iceberg (depending on the wavelength), which may lead to volume scattering or scattering from randomly oriented parts inside the ice body (e.g. ice lenses or pipes). Another explanation is the presence of multiple reflections (specifically even-bounces) with random orientations. Such multiple reflections can occur as double-bounce with the clutter surface or the presence of cracks and structures in the ice body (e.g. pinnacles). In order to have an increase of the cross-channel, the corner of the double-bounce has to have an orientation (as seen by horizontally or vertically polarized waves) different from horizontal or vertical. Interestingly, this explanation does not require the dielectric constant to be very low (i.e. dry conditions) and could be applied to wet conditions as well. This is because in wet conditions the wave penetration is very limited and the icebergs appear as a set of oriented surfaces.

The fact that the two previous explanations cover two different wetness conditions, in theory, provides the detector with a wider applicability. As a final remark, it is interesting to notice that the same observation can include two physical processes that are very different from the polarimetric point of view. Random volume scattering is an incoherent process with a low degree of polarization, while oriented even-bounce is highly coherent. This is a clear indicator that the exploitation of polarimetric data is advantageous not just to detect the icebergs, but also to retrieve geophysical parameters and/or information about the scattering and reflection processes taking place.

Two boxcar filters are applied over the HV and HH intensity images, exploiting two different window sizes: a smaller test window w_{test} and a larger training window w_{train}. Details on the dimensions are provided in next section. The detector, which we call DPolRAD, can

be written as:

$$\Lambda = \frac{\langle |HV|^2 \rangle_{test} - \langle |HV|^2 \rangle_{train}}{\langle |HH|^2 \rangle_{train}} > T_\Lambda. \quad (2)$$

where $\langle\rangle_{test}$ and $\langle\rangle_{train}$ are the spatial averages using the test and training windows respectively and T_Λ is a threshold.

To gain some physical understanding of the proposed formula, some mathematical manipulations can be carried out. If the averages are expressed explicitly the following equation can be derived (the mathematical manipulations are reported in the Appendix):

$$\Lambda = \rho_{ring} \frac{1+c}{R\rho^{-1} + cRHV^{-1}} - \rho_{train} \quad (3)$$

ρ stands for cross-over-co polarization ratio, in the following defined as depolarization ratio. The subscript is used to identify if the ρ is estimated in the ring area or the training area. The ring area is composed by the pixels of the training area that do no belong to the test area (e.g. a ring of pixels around the test area). As mentioned previously, this observable is sensitive to the presence of volume scattering or orientated structures. $R\rho$ is the ratio between the ρ inside the test area over the one in the ring around the test area (i.e. $R\rho = \frac{\rho_{test}}{\rho_{ring}}$). RHV is the ratio of the HV intensity in the test area over the ring area (i.e. $RHV = \frac{\langle |HV|^2 \rangle_{test}}{\langle |HV|^2 \rangle_{ring}}$). c is a factor such that $N_{train} = cN_{test}$ where N_{train} and N_{test} are the number of pixels inside the training and test windows. ρ_{ring} and ρ_{train} are the depolarization ratios in the ring and the entire training windows respectively.

Analyzing some special condition is possible to gain insights into the nature of the detector:

(1) It is easy to proof that Λ is equal to zero if the depolarization ratio and the HV intensity do not change between the ring and the test area. This is because $\rho_{ring} = \rho_{train}$ and

$R\rho = RHV = 1$. As a consequence, homogeneous areas will provide a Λ that is equal to zero.

(2) If and only if the depolarization ratio and the HV intensity are higher in the test area than in the ring, then Λ becomes very large. An easy way to test this is by considering the limit of $R\rho$ and RHV going to infinity:

$$\lim_{\substack{R\rho\to\infty,\\ RHV\to\infty}} \Lambda = \rho_{ring}\frac{1+c}{0+c0} - \rho_{tot} = \infty \tag{4}$$

Clearly, $R\rho$ and RHV will never reach infinity in real data due to the noise level (i.e. the values in the ring areas cannot be exactly zero).

(3) Finally, if the volume or multiple reflections decrease drastically from the ring to the test area (e.g. a pool of open water in multi-year sea ice), then Λ becomes negative. A way to see this is by analyzing the limit of Λ when $R\rho$ and RHV go to zero.

$$\lim_{\substack{R\rho\to 0,\\ RHV\to 0}} \Lambda = \rho_{ring}\frac{1+c}{\infty+c\infty} - \rho_{tot} = -\rho_{tot} \tag{5}$$

To summarize, if an iceberg of the right size enters the test window, the value of Λ increases triggering a detection. However, if the iceberg or sea ice is significantly larger than the test window it will contaminate the training window not providing a sufficient anomaly to trigger the detector. The size of the test area depends on the size of the iceberg to detect. On the other hand, the size of the training area depends on the requirement we have in detecting icebergs of a precise size. If the training window is much larger than the test window, iceberg that are slightly larger than the test window will still be detected, because the iceberg part that does not fit in the test window will be averaged out over the large training area. On the other hand, with a smaller training area, we would be more selective on the maximum size that the iceberg can have. Depending on the application (e.g. classification), this may

be important. At the moment, we are not too interested in fixing precisely the size of the iceberg and therefore we have a training area that is rather large.

As a final remark, it is interesting to notice that the same derivations can be done using the VV/VH mode, where the depolarization ratio becomes the ratio between the intensity of VH over VV. The detectors exploiting the two different modes are based on the same physical rational and therefore they are expected to have similar results. This is because HH and VV have a rather similar scattering behavior on sea ice [34], [35] with some variations that depend on the ice type. Also, icebergs are expected to scatter similarly in HH and VV, depending on ice structure. In order to evaluate if one mode is preferred to the other, a systematic analysis has to be carried out for different sea ice conditions and iceberg characteristics. In this work, we concentrate on the HH/HV mode, since this is the Sentinel-1 preferred mode for observing sea ice and it is routinely acquired in the Arctic [36].

B. Contrast enhancement

Λ is large when there is an increase in volume or multiple reflections, equals to zero on homogeneous targets and is negative if volume scattering or multiple reflections occur mainly in the ring area but are of lower magnitude in the test window. Such detector is built as a ratio between intensities and therefore it is scale invariant. This is a very valuable property for a polarimetric indicator, however scale invariance may be disadvantageous for some detection tasks. For instance, if the signal is very low and close to the noise floor, an increase in the volume component that is small in absolute magnitude may return a large Λ. An easy way to bypass this is giving the scale back by multiplying the detector by an intensity or magnitude image. In this context, the cross polarization channel should to be preferred because it shows

a higher contrast between icebergs and clutter:

$$I = \Lambda \cdot \langle |HV|^2 \rangle \tag{6}$$

In the following, we denote this expression as "HV-DePolRAD". If a pixel of the HV intensity image presents an anomaly in volume or multiple reflections, then it is multiplied by a large number. If it presents a homogeneous area, then it is multiplied by zero and if it presents a decrease in volume or multiple reflections, then it becomes negative. This enhances the contrast between anomalies in volume or multiple reflections and clutter.

C. Final remarks

As mentioned previously, the window size defines the dimension of targets (icebergs or thick/deformed ice) that can trigger the detection. Clearly, we cannot be completely sure that the detected object is an iceberg or a right-sized block of thick/deformed sea ice. However, both typologies of ice may represent hazards for the navigation and therefore it may be beneficial to detect them both.

III. Test with Real Data: RADARSAT-2

A. Data Presentation

In order to test the detector, real RADARSAT-2 and Sentinel-1 data are exploited. In this first section, results with quad-polarimetric Fine RADARSAT-2 acquisitions are presented. The latter are provided with a rather small swath width of around $25\ km$, therefore their use for operational purposes is restricted to strategic areas. The test presented here demonstrates the capabilities of the detector using image products with high spatial resolution. Moreover it is easier to identify icebergs visually and hence provide a mean of evaluating the detection

TABLE I

DETAILS ON FINE QUAD-POL RADARSAT2 DATA. TIME IS IN UTC.

Date (Time)	Location	Beam	Incidence angle	Ground range res.
27/12/2013 (09:06)	Helheim	FQ15	$\sim 35°$	9.2 m to 8.8 m
21/02/2014 (20:05)	Helheim	FQ19	$\sim 39°$	8.4 m to 8.1 m

performance. The following section deals with an exhaustive analysis of Sentinel-1 data that provides insights on actual operational conditions.

In order to increase the probability to observe icebergs, the data were acquired in the basin of the Helheim Glacier on the East Coast of Greenland. Helheim is one of the fastest calving glaciers and it finishes in a relatively long fjord, where the icebergs remain before they reach the open ocean. Moreover, the acquisitions were performed in winter, where it is expected that the fjord is covered by sea ice.

Figure 1.a and 2.a present the Pauli RGB images of the two scenes. The first exploits a FQ15 beam and it was acquired on the 27/12/2013. The second employs the FQ19 beam and it was acquired on the 21/02/2014. Table I presents the main characteristics of data exploited. Only a zoom of the second acquisition is shown here to provide a closer look at the detection masks near the melange margin.

Unfortunately, a ground survey of icebergs or thick/deformed ice is not available and we had to rely on visual inspection of the images. In particular, targets of interest were identified as bright regions in the HV channel of specific dimensions. Moreover, a shadow area in the far range and a bright rim in the near range was searched.

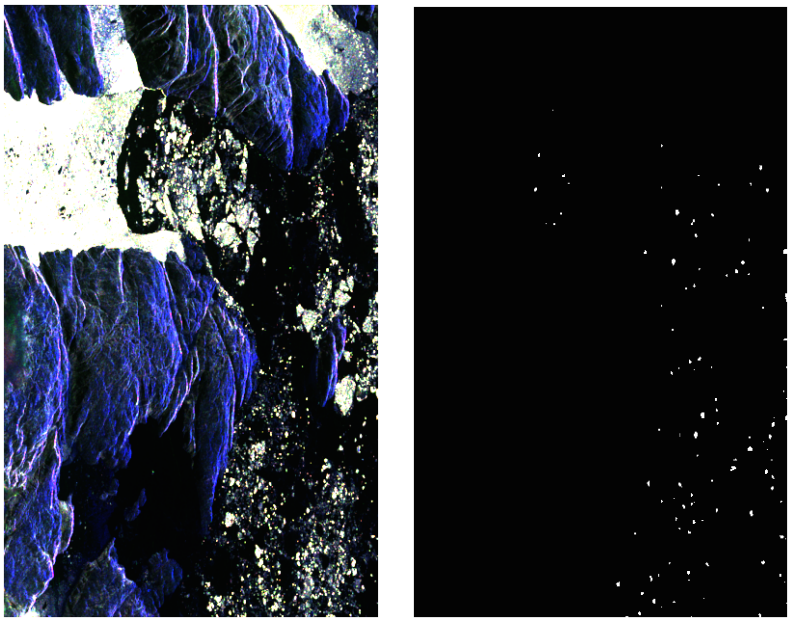

(a) Pauli RGB (b) detection mask

Fig. 1. Detection for the FQ15 27/12/2013 RADARSAT-2 dataset (Helheim, Greenland). (a) Pauli RGB image; (b) Mask with the proposed detector.

B. *Test of Detection*

The proposed algorithm only requires the intensity of HV and HH polarization channels, therefore the polarimetric capability is not fully exploited here. The window sizes used are $w_{test} = [21, 21]$ and $w_{train} = [101, 101]$ pixels. These window size are selected in order to have a test window that is in between $100\ m$ and $200\ m$ of size and it is comparable with the following tests performed with Sentinel-1 data. Figure 1.b and 2.b present the detection masks for the two areas of interest. The detection mask was obtained using thresholds on the HV-DPolRAD set locally on large training windows. More details on how to set the threshold for the HV-DPolRAD are reported in the next section. We found that all the bright and isolated areas with a specific size seem to be detected (i.e. large bright areas are rejected).

In order to provide a comparison, two detectors that consider the HV intensity alone are

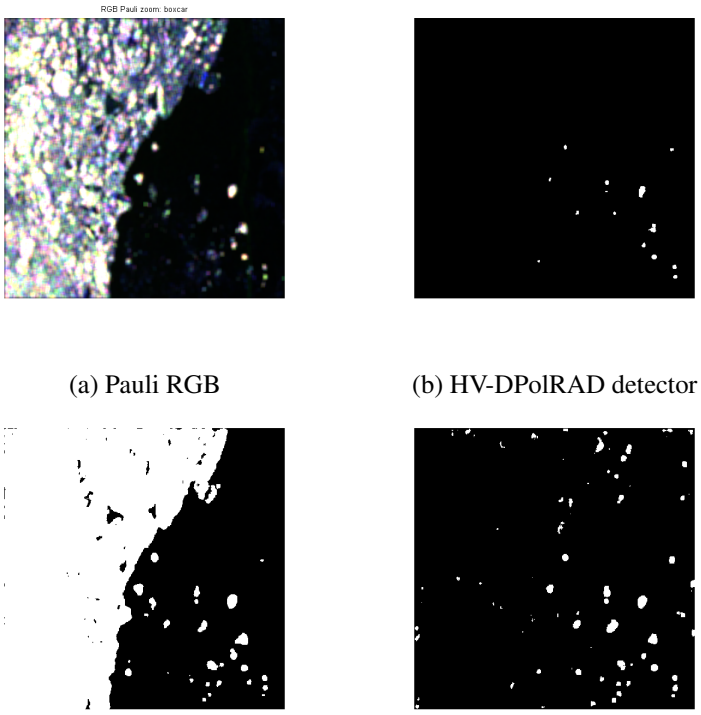

(a) Pauli RGB (b) HV-DPolRAD detector

(c) HV intensity: global threshold (d) HV intensity: local threshold.

Fig. 2. Detection for the FQ19 21/02/2014 RADARSAT-2 dataset (Helheim, Greenland). (a) Pauli RGB image; (b) Mask with the HV-DPolRAD detector; (c) Mask with the HV intensity using CFAR: $P_f = 10^{-6}$; (d) Mask with the HV intensity with empirical threshold equal to 0.1.

presented in Figure 2. The first detector sets the threshold globally using an empirical value derived by the analysis of the histogram for the large region of sea ice. The second detector sets the threshold locally exploiting ring guards (as for a CFAR methodology). The theoretical pdf used to calculate the probability of false alarms P_f is a K-distribution and the value $P_f = 10^{-6}$ is used.

It is possible to observe that the intensity alone provides several false alarms. This is due to the fact that when the clutter background has a low backscattering, several small anomalies are detected. Additionally, if the statistics are not extracted locally, large portions of sea ice are detected.

TABLE II

DETAILS ON EW SENTINEL-1 DATA.

Location	Modes	Incidence angle range	Ground range res.	Swath
East Greenland	EW HH/HV detected	$18.9°$ to $47°$	20×40 m	$400\ km$

IV. TEST WITH REAL DATA: SENTINEL-1

A. Presentation of data

In this section, the algorithm is tested using Sentinel-1 Extra Wide (EW) Swath dual-polarization images. The later provide an interesting opportunity for operational use based on their large coverage and smaller data size.

The ESA Hub archive was searched downloading images that could suite the detection exercise. We selected as test area the East Coast of Greenland, in the Fram Strait where the glaciers Helheim and Kangerdlugssuaq calve. Moreover, we selected acquisitions in the months from March to April 2015, since this should allow to monitor a relatively large amount of icebergs that are still embedded in sea ice (if not too far from the coast). Interestingly, we downloaded 31 EW dual-pol Ground Detected (GRD) acquisitions from the 1^{st} of March to the 30^{th} of April, with an average of around one image every two days. This remarkable repeat time allows to monitor the temporarily grounded icebergs, which can be easily used as validation targets.

Table II summarizes some characteristics of all the EW Sentinel-1 images exploited [37]. More details on acquisition times are provided in a following table.

Figure 3 shows the location of three of the 31 acquisitions to provide an idea of the geographical area of interest and coverage.

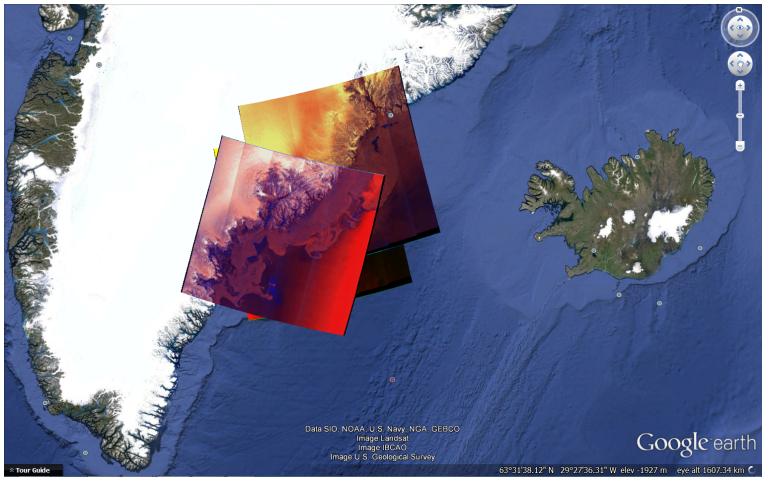

Fig. 3. Three Sentinel-1 EW acquisitions overlaid on Google Earth.

B. Visual inspection

In a preliminary analysis, few of the HH and HV magnitude images are shown. EW images have a very large coverage and presenting them in their entirety would make the identification of icebergs very challenging. For this reason, only small crops of the entire images are shown in the following.

Figure 4 and 5 present the magnitude of HH and HV for 6 different acquisitions. The images are in radar coordinates, therefore each axes represent the pixel coordinate. The first three represent an area just outside the basin where the Kangerdlugssuaq glacier calves. From the time series, it is possible to identify several bright points that move very slowly. Interestingly, some of these points cannot be detected in the HH channel, showing the importance of the cross polarized channel for iceberg detection. In particular, 10 points of the visually analyzed images appear to be stable (they are less visible in the April acquisition, maybe due to melting conditions).

A second set of images is considered to test the capability of the new detector to reject edges (the ice marginal zone) and detect icebergs embedded in bright sea ice clutter.

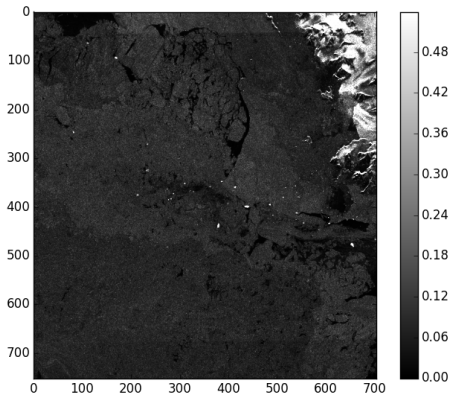

(a) HH (02/03/2015)

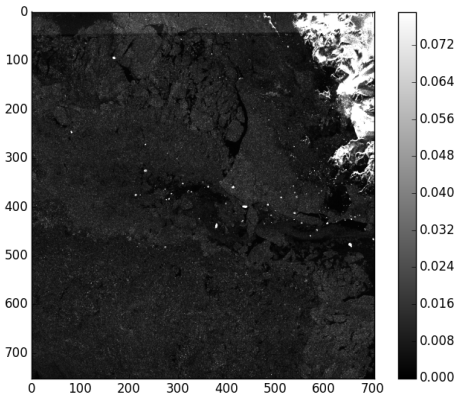

(b) HV (02/03/2015)

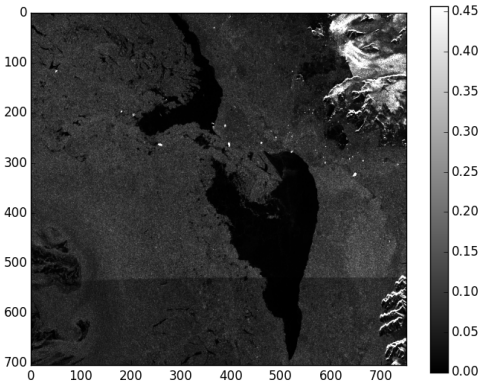

(c) HH (31/03/2015)

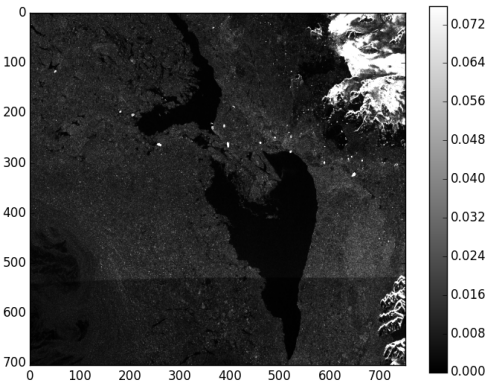

(d) HV (31/03/2015)

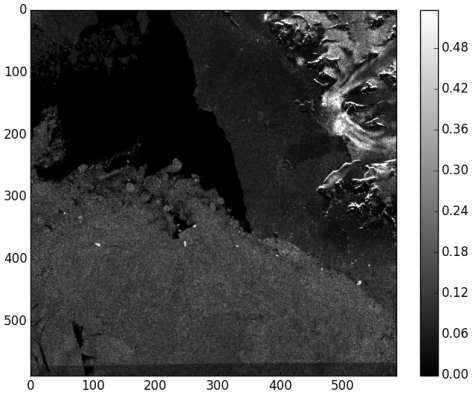

(e) HH (29/04/2015)

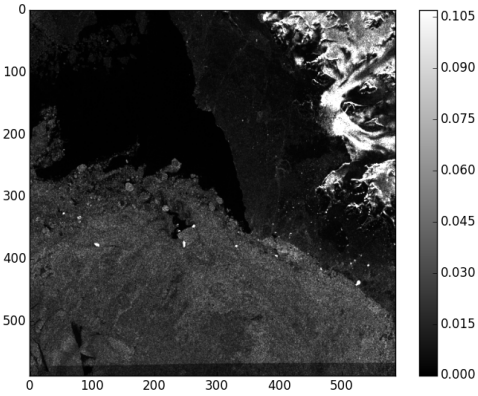

(f) HV (29/04/2015)

Fig. 4. Magnitude of HH and HV channels, Sentinel-1 EW (Kangerdlugssuaq, Greenland). (a) HH (02/03/2015); (b) HV (02/03/2015); (c) HH (31/03/2015); (d) HV (31/03/2015); (e) HH (29/04/2015); (f) HV (29/04/2015). Boxcar filter: 3×3 pixels.

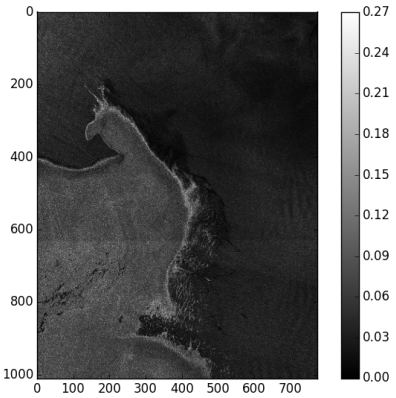

(a) HH (03/04/2015)

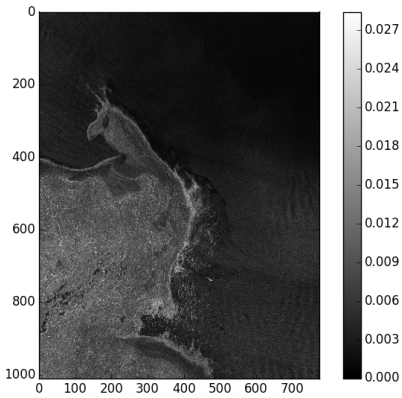

(b) HV (03/04/2015)

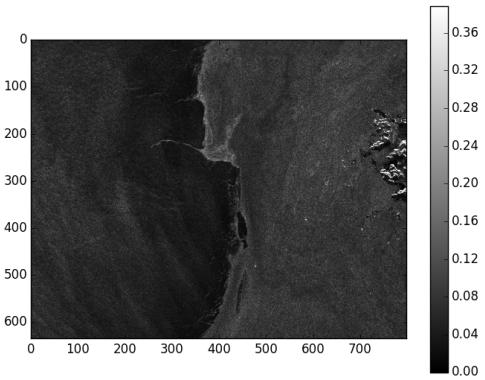

(c) HH (10/04/2015)

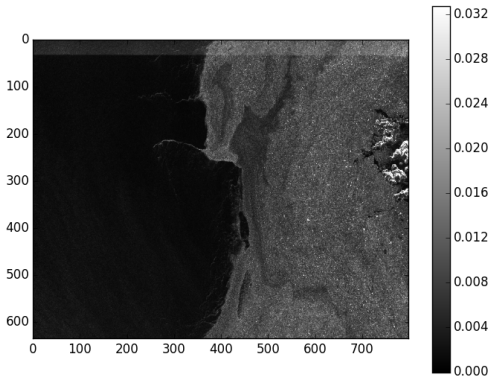

(d) HV (10/04/2015)

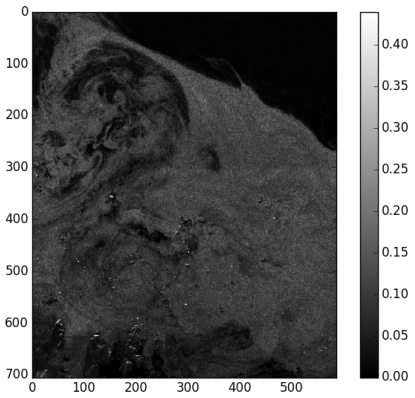

(e) HH (30/04/2015)

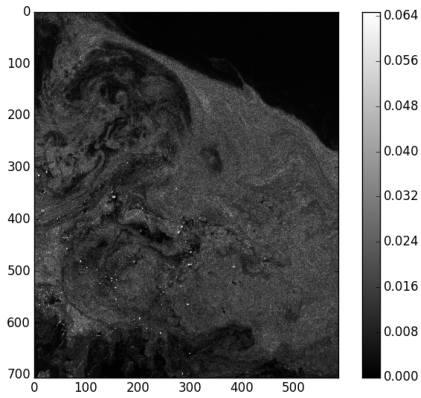

(f) HH (30/04/2015)

Fig. 5. Magnitude of HH and HV channels, Sentinel-1 EW (Fram Strait, Greenland). (a) HH (03/04/2015); (b) HV (03/04/2015); (c) HH (10/04/2015); (d) HV (10/04/2015); (e) HH (30/04/2015); (f) HV (30/04/2015). Boxcar filter: 3×3 pixels.

C. Contrast enhancement

The capability of the HV-DPolRAD to enhance the contrast between icebergs and sea ice is described in the following. The test window considers 3×3 pixels, while the training window is 63×63 pixels. The results for the 6 images are shown in Figure 6. The scaling used for these images is exactly the same as exploited for the HV magnitudes. The images appear darker, because the sea ice clutter is strongly reduced. In these images, when the DPolRAD is negative (i.e. reduction of volume or multiple reflections) the HV-DPolRAD is set to zero. On the other hand, bright isolated points remain bright. In order to have a better look at the increase in contrast, in Figure 7 the three final acquisitions are used to obtain 3D plots of the HV magnitude and the HV-DPolRAD (i.e. enhanced HV magnitude).

From the 3D plots it is evident that the clutter background is reduced and the contrast enhanced. It should be noted that the scaling between the 3D plots changes. It can be observed that several peaks are stretched upward, while the clutter is reduced. These plots are shown only for qualitative analysis and in the following a quantitative analysis is provided.

D. Detection masks

The detection masks obtained with the HV-DPolRAD are here compared with a Cell-Averaging Constant False Alarm Rate (CA-CFAR) detector. The latter extract the mean in the training window and sets the threshold equal to the mean multiplied by a factor. The factor for the CA-CFAR is selected equal to 5, since in several works, including [15], this factor has revealed to provide a good compromise between detection and false alarms. The threshold of the HV-DPolRAD is set locally (over frames of 200×200 pixels) using a CA-CFAR approach employing a factor of 50. A higher factor is used because the background is strongly reduced and we can benefit of a much higher contrast. The advantage of applying

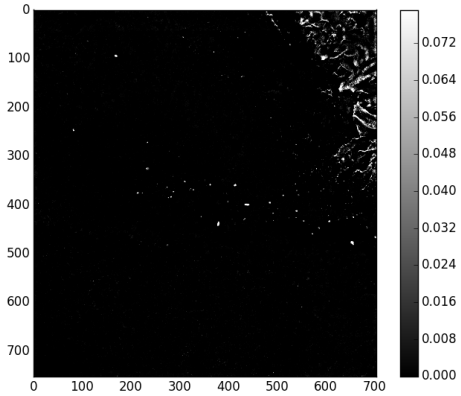

(a) HV-DPolRAD (02/03/2015)

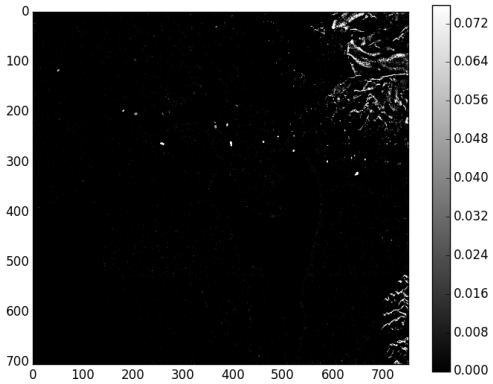

(b) HV-DPolRAD (31/03/2015)

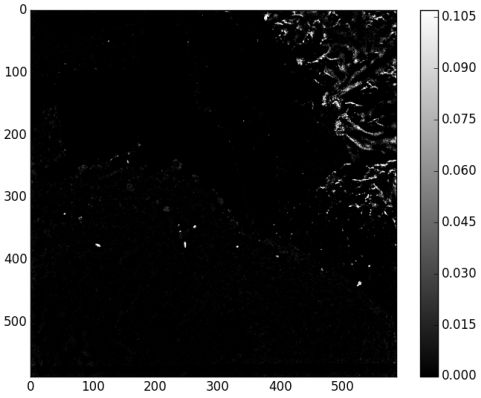

(c) HV-DPolRAD (29/04/2015)

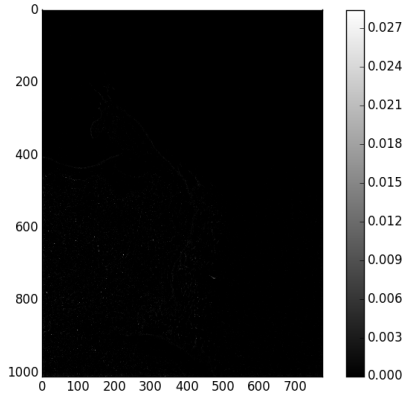

(d) HV-DPolRAD (03/04/2015)

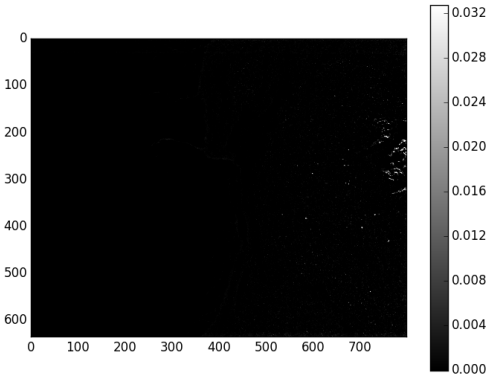

(e) HV-DPolRAD (10/04/2015)

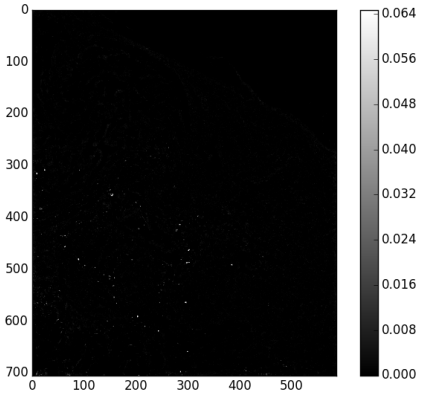

(f) HV-DPolRAD (30/04/2015)

Fig. 6. HV-DPolRAD images, Sentinel-1 EW (Fram Strait, Greenland). (a) HV-DPolRAD (02/03/2015); (b) HV-DPolRAD (31/03/2015); (c) HV-DPolRAD (29/04/2015); (d) HV-DPolRAD (03/04/2015); (e) HV-DPolRAD (10/04/2015); (f) HV-DPolRAD (30/04/2015). Boxcar filter: 3×3 pixels.

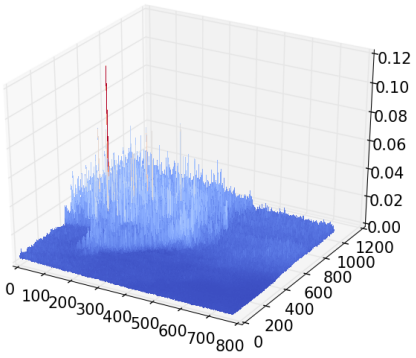

(a) HV (29/04/2015)

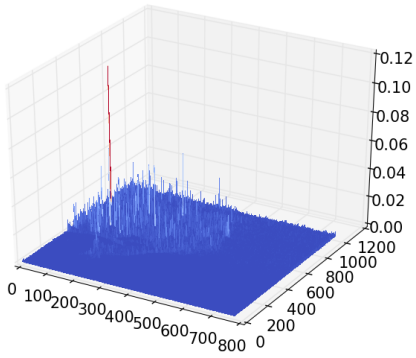

(b) HV-DPolRAD (29/04/2015)

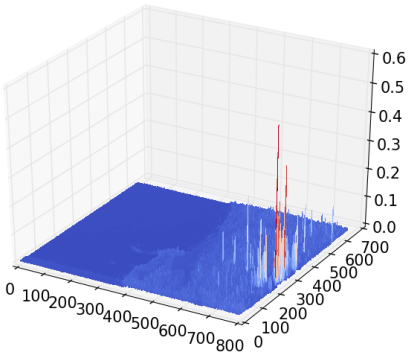

(c) HV (03/04/2015)

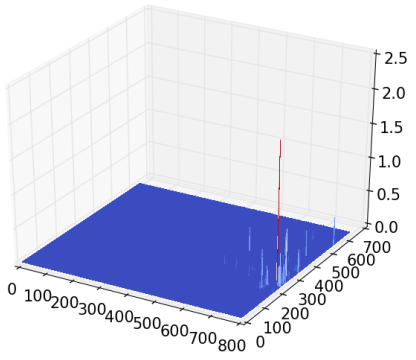

(d) HV-DPolRAD (03/04/2015)

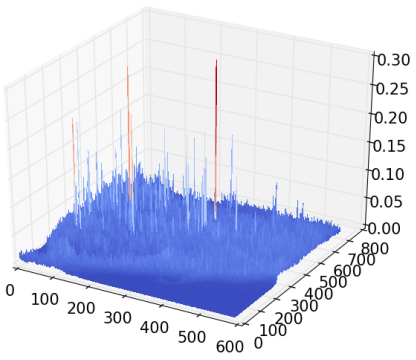

(e) HV (10/04/2015)

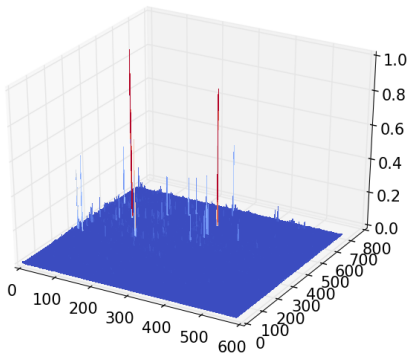

(f) HV-DPolRAD (10/04/2015)

Fig. 7. 3D plots of magnitude of HV and HV-DPolRAD (i.e. enhanced HV), Sentinel-1 EW (Fram Strait, Greenland). (a) HV (29/04/2015); (b) HV-DPolRAD (29/04/2015); (10/04/2015); (c) HV-DPolRAD (03/04/2015); (d) HV-DPolRAD (03/04/2015); (e) HV (10/04/2015); (f) HV-DPolRAD (10/04/2015). Box-car filter: 3×3 pixels. The horizontal axes are pixel coordinates and the vertical axis is pixel amplitude.

large frames instead of ring windows is that the former allow to have more clutter samples that are different from zero. In this preliminary approach, the pixels equal to zero or above a high empirical threshold are excluded to calculate the mean clutter. In the future more elaborated methods to set the threshold will be investigated. This includes the attempt to derive an analytic expression for the pdf of HV-DPolRAD.

For comparison, the CA-CFAR is applied on the HV-intensity image. Unfortunately, if we want to exploit an exact CFAR using a K-distribution (as done in the test with RADARSAT-2), the integral of the probability of false alarm has to be inverted numerically. This brings a computational burden that may be unacceptable for operational purposes with Sentinel-1 EW due to the very large amount of data to process. For this reason, the Cell-Averaging CFAR (CA-CFAR) is used and the solution of the numerical integral with a K-distribution is not attempted. This is also the reason why the CA-CFAR is so diffuse in operational algorithms. On the other hand, it is important to keep in mind that the CA-CFAR is only an approximation for the actual CFAR, which requires more powerful models to characterize the underlying statistics.

The images from the Kangerdlugssuaq glacier are analyzed first (Figure 8). The proposed algorithm is able to detect areas with possible presence of icebergs. They cluster roughly along a line and except for orientations (due to the different orbits), they preserve their distances in the two month time span. Compared to the CA-CFAR, the proposed detector is more robust against false alarms. These occur mostly in boundary regions between dark and bright clutter.

In the second series of images (Figure 9), the HV-DPolRAD seems again able to detect points that are candidate for icebergs. Some of these points appear in different images of the time series and therefore they could be attributed to grounded icebergs. These regions were

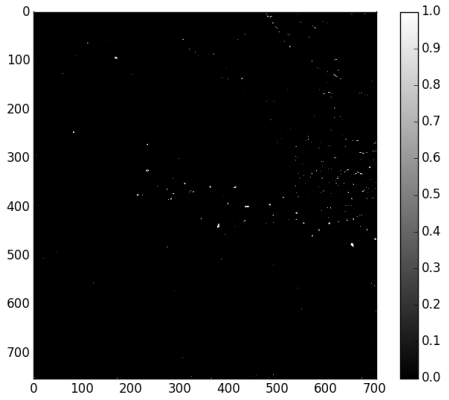

(a) CA-CFAR (02/03/2015)

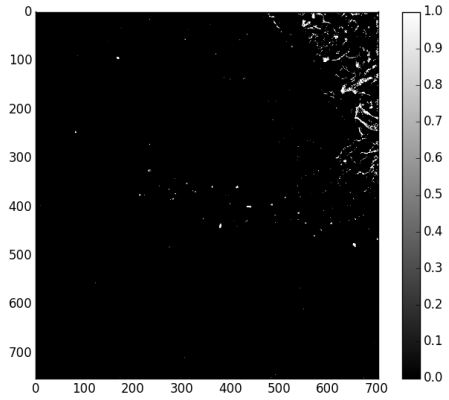

(b) HV-DPolRAD (02/03/2015)

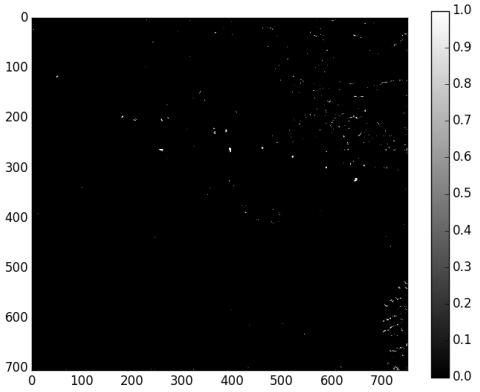

(c) CA-CFAR (31/03/2015)

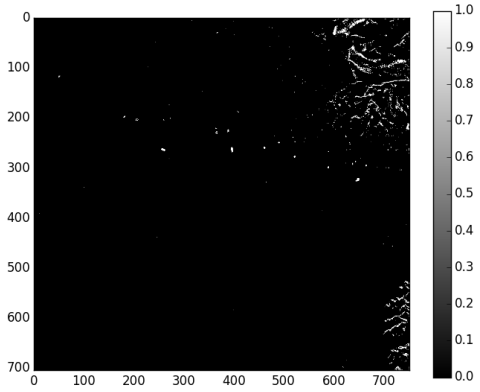

(d) HV-DPolRAD (31/03/2015)

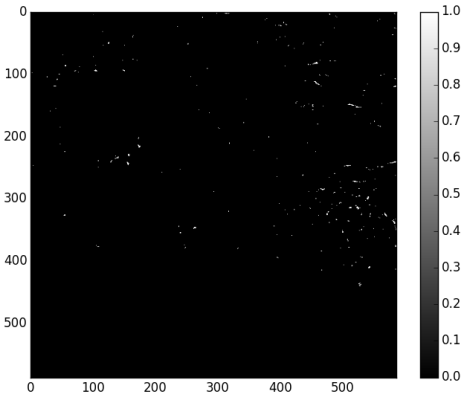

(e) CA-CFAR (29/04/2015)

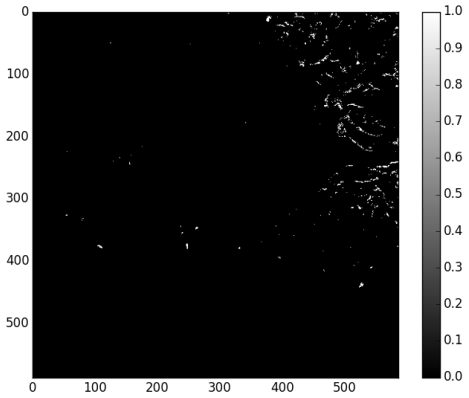

(f) HV-DPolRAD (29/04/2015)

Fig. 8. Detection masks with CA-CFAR on the HV channel and the HV-DPolRAD, Sentinel-1 EW (Kangerdlugssuaq, Greenland). (a) CA-CFAR (02/03/2015); (b) HV-DPolRAD (02/03/2015); (c) CA-CFAR (31/03/2015); (d) HV-DPolRAD (31/03/2015); (e) CA-CFAR (29/04/2015); (f) HV-DPolRAD (29/04/2015). Boxcar filter: 3×3 pixels.

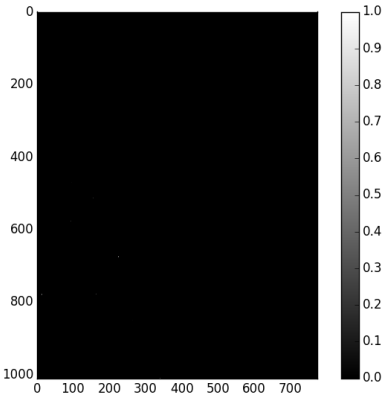

(a) CA-CFAR (03/04/2015)

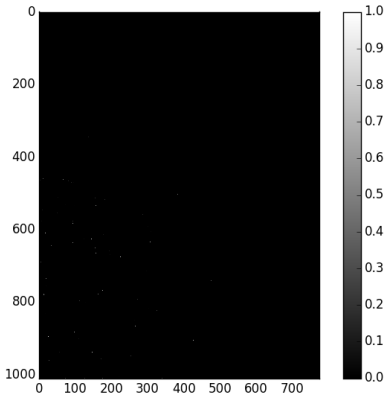

(b) HV-DPolRAD (03/04/2015)

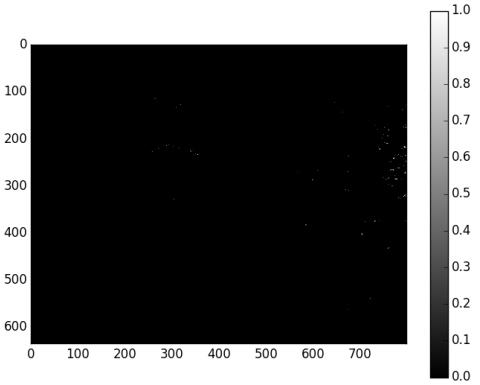

(c) CA-CFAR (10/04/2015)

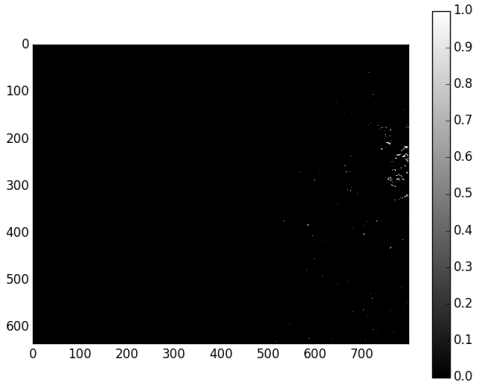

(d) HV-DPolRAD (10/04/2015)

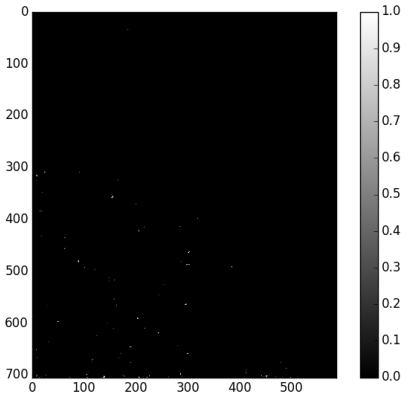

(e) CA-CFAR (30/04/2015)

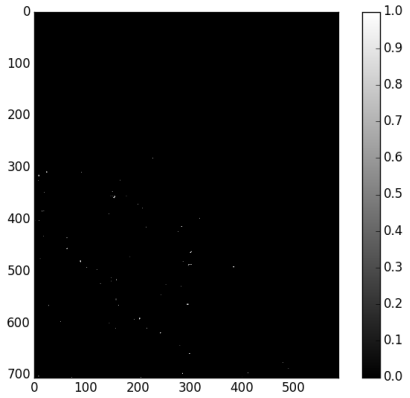

(f) HV-DPolRAD (30/04/2015)

Fig. 9. Detection masks with CA-CFAR on the HV channel and the HV-DPolRAD, Sentinel-1 EW (Fram Strait, Greenland). (a) CA-CFAR (03/04/2015); (b) HV-DPolRAD (03/04/2015); (c) HH (10/04/2015); (d) HV-DPolRAD (10/04/2015); (e) CA-CFAR (30/04/2015); (f) HV-DPolRAD (30/04/2015). Boxcar filter: 3×3 pixels.

selected because the sea ice clutter is brighter and therefore it represents a harder challenge to the detectors. Interestingly, the HV-DPolRAD is able to detect points that are missing in the CA-CFAR detection mask. This is thanks to the enhanced contrast between sea ice and icebergs.

In the future, more work will be dedicated at understanding the potentialities of proposed algorithms for operational purposes. Among other analysis, points as time burden and optimal threshold or windows selection will be tackled.

E. Quantitative analysis

In this final section, a quantitative analysis is performed. In particular, grounded icebergs can be used as validation targets. These were found not only near the basins where the Helheim and Kangerdlugssuaq glaciers calves, but also in other areas around the coastline. To extend this dataset, icebergs are searched in other areas of the dataset as well. Another indicator used to reveal the presence of icebergs is the closeness to a dark area. This can be produced by radar or wind shadow or it may be due to the fact that grounded icebergs break the surrounding sea ice and produce pools (or leads) of open water which may eventually be covered by smooth young ice under cold conditions.

The values for iceberg brightnesses used in the analysis are the ones representing the maximum inside the bright area visually identified as iceberg after the smoothing with the test window. These are the pixels that will contribute more for achieving the detection. The clutter brightnesses are estimated in each acquisition separately, using very large areas containing sea ice. In this areas, the pixels previously identified as icebergs are removed to avoid contamination of the clutter. Evaluating the clutter separately in different acquisitions allows to analyze different ice conditions separately without losing temporal information.

Tables III and IV collect results for the March and April acquisitions respectively. Each row of the table represents an acquisition. The two lines in each row indicates from which image (specified in the squared bracket) the value is taken.

The values for the HV magnitude are listed as well to provide a comparison. The tables report the minimum, maximum and mean contrast in each acquisition. In each row, the number on top represents the value for the HV magnitude and the number on bottom is for the HV-DPolRAD. It is interesting to evaluate the amount of clutter reduction compared to HV-intensity images, for the purpose of using the HV-DPolRAD images as an aid to visual inspection by analysts. The sixth column of the tables presents a comparison for the number of detected icebergs. Unfortunately, without ground surveys it is not possible to obtain any meaningful estimation of the probability of false alarms (since we do not know if a detection is genuine). The final column presents the number of icebergs used in each scene.

It is apparent that the contrast is highly improved and the clutter is strongly reduced. To visualize this result, Figure 10 plots the ratios between the HV-DPolRAD and HV mean contrasts and sea ice clutter levels. In the plot these are called "factor of improvement" since they tell how many times the contrast is increased and the clutter level is reduced. Specifically, the red curve was obtained from $\frac{meanC(HVDPolRAD)}{meanC(HV)}$, while the blue curve was calculated using $\frac{Clutter(HV)}{Clutter(HVDPolRAD)}$. In March (colder conditions) the improvement in contrast seems to be generally higher than 60 times (with few cases higher than 100). In April, the improvement in contrast is more variable and probably depends on melting conditions that makes icebergs less visible. In average, the factor of improvement is 75. Regarding the reduction of sea ice clutter, this seems to be always higher than 20 in both months and average at approximately 35.

The probability of detection for the HV-DPolRAD is always equal to one (all icebergs

TABLE III

COMPARISON OF CONTRAST. SENTINEL-1 EW HH/HV DATA. MARCH ACQUISITIONS. TIME IS IN EAST GREENLAND LOCAL TIME. MINC: MINIMUM CONTRAST; MAXC: MAXIMUM CONTRAST; MEANC: MEAN CONSTRAST; CLUTTER: MAGNITUDE OF CLUTTER LEVEL; HV: HV MAGNITUDE; DET.: NUMBER OF DETECTED ICEBERGS; TOT: TOTAL NUMBER OF ICEBERGS IDENTIFIED

Scene $[^{Date}_{Time}]$	MinC. $[^{HV}_{HVDPolRAD}]$	MaxC. $[^{HV}_{HVDPolRAD}]$	MeanC. $[^{HV}_{HVDPolRAD}]$	Clutter $[^{HV}_{HVDPolRAD}]$	Det. $[^{HV}_{HVDPolRAD}]$	Tot.
01/03/15	4	46.7	14	-19.7	38	
(08:03)	50.6	9,261	1,159	-35.3	41	41
02/03/15	5.9	43.5	18.8	-19.7	50	
(18:23)	64.3	5,009	1,454	-35.0	51	51
05/03/15	5.4	86.8	19.6	-20.1	47	
(18:48)	66.8	17,292	1,959	-35.2	48	48
07/03/15	4.2	39.9	17.2	-18.8	62	
(18:32)	54.4	5,067	1,363	-34.2	69	69
08/03/15	2.2	70.7	19.1	-20.7	44	
(07:55)	2.7	17,990	1,988	-36.5	47	47
10/03/15	1.6	67.7	17.2	-24	14	
(07:39)	32.5	11,749	1,616	-41.6	16	16
12/03/15	0.99	254	21	-21.1	69	
(18:40)	19.9	8,038	2,037	-36.3	71	71
13/03/15	5.2	64.2	18.6	-19.5	56	
(07:03)	87.7	11,530	1,455	-34.6	59	60
14/03/15	3.9	31.3	10.5	-17.8	58	
(18:24)	55.8	4,061	670	-34.8	60	60
17/03/15	4.6	45.7	16.3	-19.4	52	
(18:48)	77.5	9,484	1,436	-35.2	53	53
19/03/15	4.1	63.5	15.4	-19.5	39	
(18:32)	42.6	13,039	1,295	-34	41	41
24/03/15	4.4	38.4	17	-18.9	39	
(18:40)	51.3	4,482	1,105	-33.6	41	41
25/03/15	1.5	58.5	13.3	-19.6	38	
(08:03)	44	10,067	1,209	-35.1	39	39
26/03/15	4.2	34.8	15.4	-18.6	45	
(18:24)	47.9	4,014	1,162	-34.5	48	48
29/03/15	4.2	49.3	14.8	-19.7	52	
(18:48)	26.4	6,737	1,101	-34.6	54	54
31/03/15	4.32	47.1	18.5	-19.3	50	
(18:32)	45.9	6,115	1,252	-33.4	53	53

TABLE IV

COMPARISON OF CONTRAST. SENTINEL-1 EW HH/HV DATA. APRIL ACQUISITIONS. TIME IS IN EAST GREENLAND LOCAL TIME. MINC: MINIMUM CONTRAST; MAXC: MAXIMUM CONTRAST; MEANC: MEAN CONSTRAST; CLUTTER: MAGNITUDE OF CLUTTER LEVEL; HV: HV MAGNITUDE; DET.: NUMBER OF DETECTED ICEBERGS; TOT: TOTAL NUMBER OF ICEBERGS IDENTIFIED

Scene $\left[\frac{Date}{Time}\right]$	MinC. $\left[\frac{HV}{HVDPolRAD}\right]$	MaxC. $\left[\frac{HV}{HVDPolRAD}\right]$	MeanC. $\left[\frac{HV}{HVDPolRAD}\right]$	Clutter $\left[\frac{HV}{HVDPolRAD}\right]$	Det. $\left[\frac{HV}{HVDPolRAD}\right]$	Tot.
01/04/15	4.4	63.3	18.3	-20	21	
(07:54)	65	14,540	2,012	-34.6	25	26
03/04/15	3.9	33.3	11.5	-19.2	11	
(07:39)	43.8	4,461	773	-35.7	13	13
05/04/15	2.9	69.6	16.6	-19.6	42	
(18:40)	36.8	10,759	1,144	-33.7	45	45
07/04/15	4.6	30.2	12.7	-18.8	37	
(18:24)	54.5	2,589	650	-33.7	42	42
10/04/15	4	60.2	12.4	-19.4	40	
(18:48)	44.5	11,084	833	-34.4	43	43
12/04/15	2.1	40.0	11.0	-19.3	48	
(18:32)	30.6	6,857	981	-37	48	48
13/04/15	3.6	61.8	16.8	-20	16	
(07:55)	58.5	9,705	1,692	-35	17	17
17/04/15	2.41	37.1	9.3	-22.2	16	
(18:40)	30.6	6,112	490	-38.3	17	17
18/04/15	4.3	65.8	16.4	-21	32	
(07:03)	44	11,643	1,493	-35.9	36	36
22/04/15	2.1	22.4	9.1	-22.6	9	
(18:48)	21.2	1,339	299	-35.5	11	11
24/04/15	3.5	28.4	8.9	-18.8	15	
(18:32)	30.4	2,052	358	-33	19	19
25/04/15	2	17.4	6	-17.7	15	
(07:55)	39.6	4,233	547	-32.3	20	20
27/04/15	0.9	11.7	4.8	-18.5	15	
(07:39)	2.3	487	118	-32.3	20	20
29/04/15	2.9	19.1	8.5	-18.4	17	
(18:40)	28.4	1,329	293	-32.1	19	19
30/04/15	3.4	28	10.4	-18	25	
(08:03)	56.6	2,418	609	-32.8	27	27

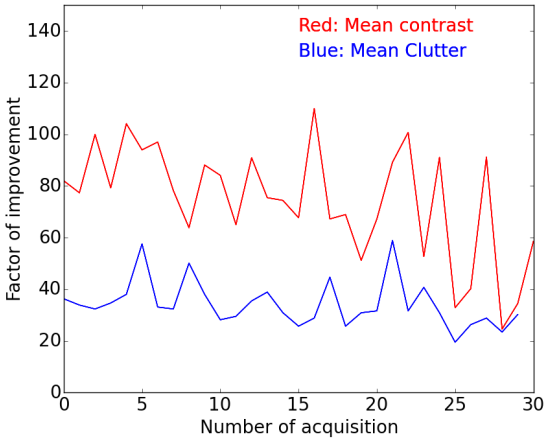

Fig. 10. Plot of contrast and clutter ratios between HV-DPolRAD and CA-CFAR over the number of acquisitions. Sentinel-1 EW (Fram Strait, Greenland). Red: ratio between HV-DPolRAD and HV magnitude mean contrast; Blue: ratio between HV-DPolRAD and HV magnitude sea ice clutter.

401 detected) at exception of two scenes where P_D is 0.99 and 0.96. This result is due to the fact
402 that in these tests we only used pixels where we have confidence of having an iceberg. It is
403 likely that our selection left out several challenging icebergs simply because we could not
404 spot them in the images. For this reason, the reported results for P_D should only be taken
405 as indicative, for the mere sake of comparison with the HV single channel. Even in this
406 simplified test, it can be observed that the HV-DPolRAD provides better detection compared
407 to the cross-pol channel alone. This is expected considering the improvement in contrast.

408 ## V. Conclusions

409 In this work, we proposed a new detector based on a new polarimetric indicator, the Dual-
410 Polarization Ratio Anomaly Detector (DPolRAD). The algorithm is focused on small ice-
411 bergs or thick/deformed ice-blocks and it is based on the combination of cross- and co-
412 polarized SAR images. In the development of the method we assumed that small icebergs
413 are contained in a limited area and they have a volume or multiple reflections contribution

that is higher compared to the surrounding sea or sea ice background. The DPolRAD is used to develop a detector called HV-DPolRAD, aimed at improving the contrast between icebergs and sea ice. The latter could also be used by ice analysis to aid visual inspection.

The detector was tested with RADARSAT-2 quad-polarimetric data and Sentinel-1 Extra Wide swath HH/HV images. We selected 31 Sentinel-1 images acquired in the East Coast of Greenland in March and April 2015. The dense time series allows to identify grounded icebergs that can be used for validation purposes.

It was observed that the HV-DPolRAD is able to improve the contrast between icebergs and sea ice compared to the HV channel alone. The improvement is in average equal to approximately 75 times. Additionally, the sea ice clutter is reduced by a factor that is in average equal to 35. The quantitative analysis showed also improved probability of detection compared to a CA-CFAR, with the HV-DPolRAD be able to detect all the identified icebergs except for two scenes.

In the future, more work will be dedicated to evaluate the potentialities of the proposed algorithms for operational use. Among other analyses, time burden and comparison of methodologies for optimal threshold and windows selection will be tackled.

APPENDIX

In this section the derivation of the formula used to gain a physical understanding of the detector is provided. We start from the expression:

$$\Lambda = \frac{\langle |HV|^2 \rangle_{test} - \langle |HV|^2 \rangle_{tr}}{\langle |HH|^2 \rangle_{tr}} \tag{7}$$

If $\frac{\langle |HV|^2 \rangle_{tr}}{\langle |HH|^2 \rangle_{tr}} = \rho_{tr}$ we can rewrite Λ as:

$$\Lambda = \frac{\langle |HV|^2 \rangle_{test}}{\langle |HH|^2 \rangle_{tr}} - \rho_{tr}$$

The averaging can be represented as the sum of the pixels inside an averaging window, divided by the total number of pixels considered. This is $\langle |HV_i|^2 \rangle_{test} = \frac{1}{N_{test}} \sum_{i=1}^{N_{test}} |HV_i|^2$. Additionally, the training window is composed by the test window plus a ring of pixels around the test window. Applying these two manipulations to the previous formula we obtain:

$$\begin{aligned} \Lambda &= \frac{\sum_{i=1}^{N_{test}} |HV_i|^2}{N_{test}} \frac{N_{test} + N_{ring}}{\sum_{i=1}^{N_{test}} |HH_i|^2 + \sum_{i=1}^{N_{ring}} |HH_i|^2} - \rho_{tr} \\ &= \frac{\sum_{i=1}^{N_{test}} |HV_i|^2}{\sum_{i=1}^{N_{test}} |HH_i|^2 + \sum_{i=1}^{N_{ring}} |HH_i|^2} \frac{N_{test} + N_{ring}}{N_{test}} - \rho_{tr}. \end{aligned} \tag{8}$$

If we define $N_{ring} = cN_{test}$ the equation can be written as:

$$\Lambda = \frac{1+c}{\frac{\sum_{i=1}^{N_{test}} |HH_i|^2}{\sum_{i=1}^{N_{test}} |HV_i|^2} + \frac{\sum_{i=1}^{N_{ring}} |HH_i|^2}{\sum_{i=1}^{N_{test}} |HV_i|^2}} - \rho_{tr}$$

Going back with the representation with angular brackets and considering the definition of the depolarization ratio the following expression can be written:

$$\Lambda = \frac{1+c}{\rho_{test}^{-1} + \frac{\langle |HH|^2 \rangle_{ring} N_{ring}}{\langle |HV|^2 \rangle_{test} N_{test}}} - \rho_{tr}$$

If we define the ratio between the HV intensity of the test area over the ring area as $RHV = \frac{\langle |HV|^2 \rangle_{test}}{\langle |HV|^2 \rangle_{ring}}$ the expression can be modified as:

$$\Lambda = \frac{1+c}{\rho_{test}^{-1} + \frac{c}{RHV\,\rho_{ring}}} - \rho_{tr}$$

Additionally we can define the ratio between the polarization ratio in the test over the ring area as $\rho_{test} = \rho_{ring} R\rho$. The expression becomes:

$$\Lambda = \frac{1+c}{\rho_{ring}^{-1} R\rho^{-1} + c\rho_{ring}^{-1} RHV^{-1}} - \rho_{tr} \tag{9}$$

$$= \rho_{ring} \frac{1+c}{R\rho^{-1} + cRHV^{-1}} - \rho_{tr},$$

which is the final expression.

ACKNOWLEDGMENT

RADARSAT-2 Data and Products ©MacDonald, Dettwiler and Associates Ltd. (2013-2014) - All Rights Reserved. RADARSAT is an official trademark of the Canadian Space Agency. Sentinel-1 data were used courtesy of the European Space Agency. The data were downloaded from the Sentinel Hub website. Armando Marino would like to thank Romina Rulli for her help testing a preliminary version of the detector on RADARSAT-2 data, Irena Hajnsek (ETH Zurich and DLR) for the encouragement and support of the initial version of the detector and Kostas Papathanassiou (DLR) for some enjoyable talk about observing depolarization.

REFERENCES

[1] I. H. Woodhouse, *Introduction to Microwave Remote Sensing*, CRC Press, 2004.

[2] A. L. Gray and L. D. Arsenault, "Time-delayed reflections in L-band synthetic aperture radar imagery of icebergs," *IEEE Transactions on Geoscience and Remote Sensing*, vol. 29, no. 2, pp. 284–291, Mar. 1991.

[3] J.-W. Kim, D.-J. Kim, S.-H. Kim, and B.-J. Hwang, "Iceberg detection using full-polarimetric RADARSAT-2 SAR data in West Antarctica.," *Proc. 3rd Intrnation APSAR conference*, pp. 1–4, Sept. 2011.

[4] W. Dierking and C. Wesche, "C-Band radar polarimetry - useful for detection of icebergs in sea ice?," *IEEE Transactions and Geoscience and Remote Sensing*, vol. 52, no. 1, pp. 25–37, Jan 2014.

[5] H.D. Pritchart, R.J. Arthern, D.G. Vaughan, and L.A. Edwards, "Extensive dynamic thinning on the margins of the greenland and antarctic ice sheet," *Nature*, vol. 461, pp. 971–975, 2009.

[6] T. Murray, N. Selmes, T.D. James, S. Edwards, I. Martin, T. O'Farrell, R. Aspey, I. Rutt, M. Nettles, and T. Baugé, "Dynamics of glacier calving at the ungrounded margin of helheim glacier, southeast greenland," *Journal of Geophysical Research Earth Surface*, vol. 120, no. 6, pp. 964–982, 2015.

[7] C. Wesche and W. Dierking, "Iceberg signatures and detection in synthetic aperture radar (SAR) images in two test regions of the Weddell Sea, Antarctica," *Journal of Glaciology*, vol. 58, no. 208, pp. 325–339, 2012.

[8] D. Power, J. Youden, K. Lane, C. Randell, and D. Flett, "Iceberg detection capabilities of RADARSAT synthetic aperture radar.," *Canadian Journal of Remote Sensing*, vol. 27, no. 5, pp. 476–486, Oct. 2001.

[9] R.S. Gill, "Operational detection of sea ice edges and icebergs using SAR," *Canadian Journal of Remote Sensing*, vol. 27, no. 5, pp. 411–432, 2001.

[10] V. A. Abramov, "Russian iceberg observations in the barents sea, 1933-1990," *Polar Research*, vol. 11, no. 2, pp. 93–97, 1992.

[11] J. Buus-Hinkler, K. Qvistgaard, and K. A. Harnvig Krane, "Iceberg number density - reaching a full picture of the greenland waters," *IEEE Geoscience and Remote Sensing Symposium (IGARSS)*, pp. 270–273, 2014.

[12] "C-core: https://www.c-core.ca/icebergsurveillance," 2015.

[13] M. Andres, A. Silvano, F. Straneo, and D. R. Watts, "Iceberg and sea ice detected with inverted echo sounders," *Journal of Atmospheric and Oceanic Technology*, vol. 32, pp. 1042–1057, 2015.

[14] S. M. Kay, *Fundamentals of Statistical Signal Processing*, Prentice Hall, Upper Saddle River, US, 1993.

[15] D. J. Crisp, "The State-of-the-Art in ship detection in Synthetic Aperture Radar imagery," *Australian Government Department of Defence*, 2004.

[16] K. Eldhuset, "An automatic ship and ship wake detection system for spaceborne SAR images in coastal regions," *IEEE Transactions on Geoscience and Remote Sensing*, vol. 34, no. 4, pp. 1010 – 1019, July 1996.

[17] P. W Vachon, "Ship detection in synthetic aperture radar imagery," *Proceedings OceanSAR, St. John s, NL, Canada*, 2006.

[18] C.C. Wackerman, K.S. Friedman, W.G. Pichel, P. Clemente-Colon, and X. Li, "Automatic detection of ships in RADARSAT-1 SAR imagery," *Canadian Journal of Remote Sensing*, vol. 27, 2001.

[19] M. Yeremy, G. Geling, M. Rey, B. Plache, and M. Henschel, "Results from the CRUSADE ship detection trial: polarimetric SAR," *Proceeding on IGARSS 2002, Toronto, Canada, 24-28 June*, 2002.

[20] M. Brizi, P. Lombardo, and D. Pastina, "Exploiting the shadow information to increase the target detection performance in SAR images," *International Conference on Radar Systems, RADAR 1999. Brest, Germany, April*, 1999.

[21] K.S. Friedman, C. Wackerman, Funk, W.G. Pichel, P. Clemente-Colon, and X. Li, "Validation of a CFAR vessel detection algorithm using known vessel locations," *IEEE 2001 International Geoscience and Remote Sensing Symposium (IGARSS'01), 9-13 July*, vol. 4, pp. 1804–1806, 2001.

[22] G. Margarit, J. A. Barba Milanés, and A. Tabasco, "Operational ship monitoring system based on synthetic aperture radar processing," *Remote Sensing*, vol. 1(3), pp. 375–392, 2009.

[23] P. Iervolino, R. Guida, and P. Whittaker, "NovaSAR-S and maritime surveillance," *IEEE Geoscience and Remote Sensing Symposium, 21-26 July, Melbourne, Australia*, 2013.

[24] S. R. Cloude, *Polarisation: Applications in Remote Sensing*, Oxford University Press, Oxford, UK, 2009.

[25] F. Nunziata, M. Migliaccio, and C.E. Brown, "Reflection symmetry for polarimetric observation of man-made metallic targets at sea," *IEEE Journal of Oceanic Engineering*, vol. 37, no. 3, pp. 384–394, July 2012.

[26] R. Shirvany, M. Chabert, and J.-Y. Tourneret, "Ship and oil-spill detection using the degree of polarization in linear and hybrid/compact dual-pol SAR," *IEEE Journal of Selected Topics in Applied Earth Observations and Remote Sensing*, 2012.

[27] R. Touzi, "On the use of polarimetric SAR data for ship detection," *IGARSS Geoscience and Remote Sensing Symposium*, vol. 2, pp. 812–814, 1999.

[28] W.L. Cameron, N.N. Youssef, and L.K. Leung, "Simulated polarimetric signatures of primitive geometrical shapes," *IEEE Transactions on Geoscience and Remote Sensing*, vol. 34, no. 3, pp. 793–803, May 1996.

[29] D. Velotto, F. Nunziata, M. Migliaccio, and S. Lehner, "Dual-polarimetric TerraSAR-X SAR data for target at sea observation," *IEEE Geoscience and Remote Sensing Letters*, vol. 10, no. 5, pp. 1114–1118, Sep. 2013.

[30] A. Marino, M. Sugimoto, K. Ouchi, and I. Hajnsek, "Validating a notch filter for detection of targets at sea with ALOS-PALSAR data: Tokyo Bay," *IEEE Journal of Selected Topics in Applied Earth Observations and Remote Sensing*, vol. 7, no. 12, pp. 4907–4918, Dec. 2014.

[31] A. Marino, "A notch filter for ship detection with polarimetric SAR data," *IEEE Journal of Selected Topics in Applied Earth Observations and Remote Sensing*, vol. 6, no. 3, pp. 1219 – 1232, June 2013.

[32] A. Marino and I. Hajnsek, "Iceberg detection with TerraSAR-X data using a Polarimetric Notch Filter," *IGARSS'12, Munich, Germany*, 2012.

[33] ESA, "Esa copernicus: http://www.esa.int/our_activities/observing_the_earth/copernicus/sar_missions," 2015.

[34] R. D. Drinkwater, R. Kwok, D. P. Winebrenner, and E. Rignot, "Multifrequency polarimetric synthetic aperture radar observations of sea ice," *Journal of Geophysical Research Oceans*, vol. 96, no. C11, pp. 20679–20698, Nov. 1991.

[35] M. J. Manore, D. G. Flett, R. A. De Abreu, and B. R. Ramsay, "Multi-polarization SAR data for operational ice monitoring," *IEEE 2001 International Geoscience and Remote Sensing Symposium (IGARSS'01), 9-13 July, Sydney Australia*, vol. 3, pp. 1246–1248, July 2001.

[36] P. Potin, B. Rosich, and S. Schmuck, "Sentinel-1 mission operations concept," *SEASAR 2012, Tromso, Norway*, 2012.

[37] ESA, "Sentinel-1 ew: https://sentinel.esa.int/web/sentinel/user-guides/sentinel-1-sar/acquisition-modes/extra-wide-swath," .